

Thermomechanical properties of amorphous metallic tungsten-oxygen and tungsten-oxide coatings

E. Besozzi^a, D. Dellasega^{a,b}, V. Russo^a, M. Passoni^{a,b}, M.G. Beghi^a

^a *Dipartimento di Energia, Politecnico di Milano, via Ponzio 34/3, I-20133, Milano, Italy*

^b *Associazione EURATOM-ENEA, IFP-CNR, Via R. Cozzi 53, 20125 Milano, Italy*

Abstract

In this work, we investigate the correlation between morphology, composition, and the mechanical properties of metallic amorphous tungsten-oxygen and amorphous tungsten-oxide films deposited by Pulsed Laser Deposition. This correlation is investigated by the combined use of Brillouin Spectroscopy and the substrate curvature method. The stiffness of the films is strongly affected by both the oxygen content and the mass density. The elastic moduli show a decreasing trend as the mass density decreases and the oxygen-tungsten ratio increases. A plateau region is detected in correspondence of the transition between metallic and oxide films. The compressive residual stresses, moderate stiffness and high local ductility that characterize compact amorphous tungsten-oxide films make them promising for applications involving thermal or mechanical loads. The coefficient of thermal expansion is quite high (i.e. $8.9 \cdot 10^{-6} \text{ K}^{-1}$), being strictly correlated to the amorphous structure and stoichiometry of the films. Under thermal treatments they show a quite low relaxation temperature (i.e. 450 K). They crystallize into the γ monoclinic phase of WO_3 starting from 670 K, inducing an increase by about 70% of material stiffness.

Keywords: Tungsten oxide coatings, thermomechanical properties, residual stresses, thermal expansion coefficient, thermal stability

1. INTRODUCTION

Amorphous metallic tungsten-oxygen (W-O) and amorphous tungsten-oxide (WO_x) coatings are investigated for a wide range of applications. Compact amorphous WO_3 films with tuned electrical and optical properties are usually exploited for electrochromic devices [1, 2, 3], as contact electrodes in advanced solar cell research [1, 4, 5] and for smart windows [6]. Porous WO_3 films, due to their high active area for chemical and physical reactions, are commonly adopted for photoelectrochemical water splitting [7, 8] and photocatalysis [9, 10]. Finally, metallic amorphous tungsten films with a high oxygen content (i.e. W-O) can be annealed in a reducing atmosphere to produce, in an alternative way, tungsten-oxide nanowires, which show unique electric and electrochromic properties useful for gas sensors and catalysis [11, 12]. The functional properties of these films strictly depend on the specific morphology, structure and stoichiometry, thus demanding a strong characterization effort.

Among all the functional properties, the investigation of the correlation between the thermomechanical properties, the structure, the morphology and the composition of the materials is fundamental when dealing with coatings. For example, compressive or tensile residual stresses can alter the behavior of the films in their operation environments by mitigating or favoring cracks formation or, in high tem-

perature applications, a high coefficient of thermal expansion mismatch between the coating and the substrate can instead result in high interface stresses, with possible coating delamination and device failure. Moreover, some applications (e.g. solar-cells, thermophotovoltaic) require tungsten oxide coatings to operate at a certain temperature that can be different from room temperature [13]. This could induce, for example, phase transition or recrystallization, with a consequent variation of the as-deposited properties. The knowledge of these properties together with the elastic moduli of the films is thus mandatory to determine the optimal material properties for the realization of stable and reliable devices. Until now, however, very few works aimed at relating the nanostructure and the composition of W-O and WO_x films to their mechanical properties [14, 15, 16]. The goal of this work is thus to achieve a satisfactory comprehension of the effects of structures, morphologies and chemical compositions on the thermomechanical properties of different systems of amorphous W-O and WO_x coatings, providing useful results for devices fabrication. We derive the residual stresses (σ_{res}), the elastic moduli, the coefficient of thermal expansion (*CTE*) and the total stresses (σ_f) of amorphous films characterized by different oxygen/tungsten ratios (i.e. metallic/oxide) and morphologies (i.e. compact and porous). We also assess their thermal stability under high temperatures, investigating the crystallization process of the amor-

phous phase and the induced changes on the elastic properties.

The investigated coatings are deposited by Pulsed Laser Deposition (PLD), which, as described in our past works [17, 18, 19], allows a significant versatility in tailoring the structure, the morphology and the O₂ enrichment of the deposited samples. For the thermomechanical characterization we exploit Brillouin spectroscopy (BS) and the substrate curvature method (SC). The coupling of these two techniques has been shown to be a powerful tool for the characterization of nanostructured films, providing a broad, non destructive characterization of the samples [20, 21, 22]. In particular, when transparent oxide coatings are investigated, BS can be able to derive, through the detection of surface and bulk acoustic waves, all the elastic moduli of the films (i.e. Young Modulus (E), shear modulus (G), bulk modulus (K) and Poisson's ratio (ν)) at the same time [23, 24]. SC, instead, can be exploited to measure the residual stresses of the coatings. In addition, if SC measurements are performed during annealing treatments, also the coefficient of thermal expansion (CTE) and the total stress evolution (σ_f) of the film can be derived [22]. The influence of high temperatures on the properties (i.e. elastic moduli, structure and morphology) of the films is finally assessed by thermal annealing treatments at various temperatures up to 870 K. The variation of σ_f over temperature is thus monitored by the SC setup, in order to derive information about material stress evolution. The stoichiometry, structure and morphology are monitored by Raman spectroscopy, Scanning Electron Microscopy (SEM) and Energy Dispersive X-Ray Spectroscopy (EDXS).

2. EXPERIMENTAL

2.1. Deposition, structure, morphology and composition characterization

The coatings analyzed in this work are deposited by the same PLD apparatus described in details in [17, 18]. It consists in a Nd:YAG laser (pulse duration $\tau_p = 7$ ns (FWHM)), operating at its 2nd harmonic ($\lambda = 532$ nm), focused on a W target (purity 99.9%). The repetition rate is 10 Hz, the laser energy ≈ 800 mJ and the laser spot about 9.2 mm². The fluence (F) on target is thus ≈ 15 J cm⁻². W ablated species expand into a vacuum chamber (base pressure of $\approx 10^{-3}$ Pa) in presence of O₂ as background gas, with a pressure which is varied between 5 and 60 Pa. The films are deposited onto 300 μ m thick Si(100) substrates. These substrates are double side polished for SC measurements.

Structural and morphological properties are assessed by a Zeiss Supra 40 field emission Scanning Electron Microscope (SEM), operating at an accelerating voltage of 5 kV, and by micro-Raman measurements, with a Renishaw InVia spectrometer equipped with an Ar⁺ laser ($\lambda = 514.5$ nm), a 1800 g/mm grating and an edge filter with cut at

100 cm⁻¹. The laser is set to operate at 1 mW continuum power through a 50X objective to avoid any local material modification. The composition of the samples is determined by Energy Dispersive X-ray Spectroscopy (EDXS) in the same SEM system, working with an accelerating voltage of 15 kV in order to promote the excitation of K _{α} and M _{α} electronic shells of W and O. Each measurement is repeated three times in different points of the samples, with a total integrated counts number of 2×10^5 for each point. Finally, the mass density of the deposited films is evaluated by combining weight measurements before and after the deposition using a precision balance (i.e. 10⁻⁴ g) and SEM cross-section for thickness determination.

2.2. Elastic moduli characterization

The elastic moduli of the coatings are evaluated by the BS spectroscopy setup described in [20], with a Nd:YAG laser (continuum operation at ≈ 200 mW, $\lambda = 532$ nm) focused on the coating surface. The scattered light is collected in the backscattering geometry without polarization analysis by a Fabry-Perot multi-pass interferometer, operating in the tandem mode, of the Sandercock type.

In the case of sufficiently transparent materials light can be inelastically scattered by bulk ultrasonic waves, by the *elasto-optic mechanism* (the modulation of the refractive index by a mechanical strain). The properties of bulk waves are thus accessible [23]. At the free surface of solids Surface Acoustic Waves (SAWs) also exist, whose displacement field is confined in the vicinity of the surface, and declines with depth, the decay length being close to the wavelength. In the case of metallic samples light cannot penetrate, and interacts only with the SAWs: the process is mediated by the *surface ripple mechanism*, i.e. the dynamic corrugation of the surface due to the wave displacement. The properties of SAWs are thus accessible [20]. Since the properties of both bulk waves and SAWs depend on the mass density and the elastic properties, in both cases the elastic properties can be derived as it follows.

Under the assumption of a homogeneous isotropic linear elastic medium, the elastic stiffness tensor is defined by only two independent constants, namely C_{11} and C_{44} . All the elastic moduli can be, then, expressed in terms of these two elastic constants. Surface waves simultaneously contain information about C_{11} and C_{44} . If only SAWs are detected, a suitable procedure must be adopted in order to derive C_{11} and C_{44} . This method is described in detail in [20]. It consists in recording the spectra at different incidence angles θ , such that an experimental dispersion relation of the modes, as function of θ , i.e. of wave vector k , can be obtained. A least squares minimization between the measured experimental dispersion relations and the theoretical ones is then computed. Theoretical dispersion relations are computed by solving the Christoffel's secular equation for an equivalent homogeneous system under the isotropic assumption. The minimization is performed with C_{11} and C_{44} as the only free parameters, such as the most

probable estimates for C_{11} and C_{44} are obtained. The number of the experimental observed peaks determines, in turn, the accuracy in the determination of the elastic properties of the films [20]. When bulk modes can be detected a higher amount of elastic information can be extracted. In this case C_{11} and C_{44} are associated to the velocities of the bulk waves as [24]:

$$v_L = \sqrt{\frac{C_{11}}{\rho}} \quad (1)$$

$$v_T = \sqrt{\frac{C_{44}}{\rho}} \quad (2)$$

where v_L and v_T can be, in turn, directly computed from the frequency shifts ($\Delta\omega$) of the bulk peaks in the Brillouin spectra as:

$$v_{L,T} = \frac{\Delta\omega_{L,T}\lambda_0}{4\pi n} \quad (3)$$

In equation 3, λ_0 is the laser wavelength and n the refractive index of the material [24]. As it can be seen, in this case, to obtain v_L and v_T both the refractive index and the mass density of the coatings must be known. As it will be discussed in section 3.2, n will be estimated directly from Brillouin spectra.

2.3. Residual stresses, CTE and annealing treatments

Residual stresses are measured by an optical implementation of the SC method. The system exploits a set of parallel laser beams to probe the curvature radius of the coating-substrate system. The laser apparatus is implemented into an ad-hoc developed experimental setup, fully described in [22]. The scanned area is $\approx 1 \text{ cm}^2$ and the laser beams strike on the uncoated substrate surface before being collected by a high frame rate camera. Residual stresses are derived by measuring the variation of the substrate curvature before and after films deposition and by applying the Stoney's approximation. This approximation says that for a thin supported film the residual stress σ_{res} can be computed for the wafer curvature as [25]:

$$\sigma_{res} = \frac{E_s}{1 - \nu_s} \frac{t_s^2}{t_f} \frac{1}{6R_c} \quad (4)$$

where E_s and ν_s are the Young modulus and Poisson's ration of the substrate, t the thicknesses of the and the substrate and R_c the total curvature of the system. In this case, R is measured multiple times on the same sample varying the probed position.

Standard thermal annealing treatments are performed in the same apparatus of SC, exploiting a resistive heater stage. The temperature ranges between room temperature (RT) and 870 K. All treatments are performed for 1 h (i.e. dwell annealing time) in vacuum (i.e. base pressure of $\approx 10^{-4}$ Pa), in order to in principle avoid any modification of the composition. The heating ramp is set to ≈ 3

- 5 K min^{-1} . The temperature is measured by a thermocouple placed beneath the sample.

The thermal stress evolution and the CTE, instead, are obtained by monitoring the substrate curvature change of the film-substrate system during fast heating ramps ($\approx 50 \text{ K min}^{-1}$) in the same SC apparatus, again under Stoney's assumption. In this case, the substrate curvature is measured by fixing the position of the laser beams. R_c is monitored during heating and cooling and the resulting stress is computed by equation 4. Under the assumption of uniform material temperature the thermal stress can be computed as:

$$\sigma_f = \frac{E_f}{1 - \nu_f} (CTE_f - CTE_s) \Delta T \quad (5)$$

Equation 4 and 5 are compared such as the CTE of the film can be derived. For this type of measurements a high acquisition frame rate (i.e. 7 fps) is exploited to have sufficient data for successive statistical manipulations. The performances of the setup and more details on the measurements procedure can be found in [22].

3. RESULTS AND DISCUSSION

3.1. Structure, morphology and composition of amorphous W-O and WO_x coatings

In this section, we show the structure, the morphology and the composition of the analyzed films, which are fundamental for the contextualization of the thermomechanical properties. A detailed description of the growth process of these coatings by PLD can be found elsewhere [17, 18]. Plane views and cross-section SEM images of the analyzed samples are shown in figure 1. Samples produced at O_2 pressure below 20 Pa are characterized by a compact structure. At 20 Pa a compact nanostructured morphology appears. At higher pressures, instead, an open porous morphology prevails. As it can be seen, at 60 Pa the pressure is sufficiently high to start promoting *cauliflower* growth. These different morphologies are related to distinct growth mechanisms, as reported in [17, 18], strictly correlated to the expansion dynamic of the plasma plume during deposition. Low O_2 pressures promote atom-by-atom deposition, that results in the growth of compact films, while high O_2 pressures favors clusters formation inside the plume, so a porous morphology.

The O/W stoichiometric ratio, which is assessed by EDXS analysis, is in turn affected by the deposition pressure. The ratios are summarized in table 1. As it can be seen, we have O/W ≈ 2.1 at 5 Pa, increasing to ≈ 2.6 at 15 Pa. Above 20 Pa, instead, the films are almost stoichiometric WO_3 . This can be associated again to an increase of interactions probability between W and O inside the plasma plume at sufficiently high O_2 pressures.

The structure of the films is investigated by Raman spectroscopy reported in figure 2. All the spectra show two broad bands, a low frequency band in the range of 100 -

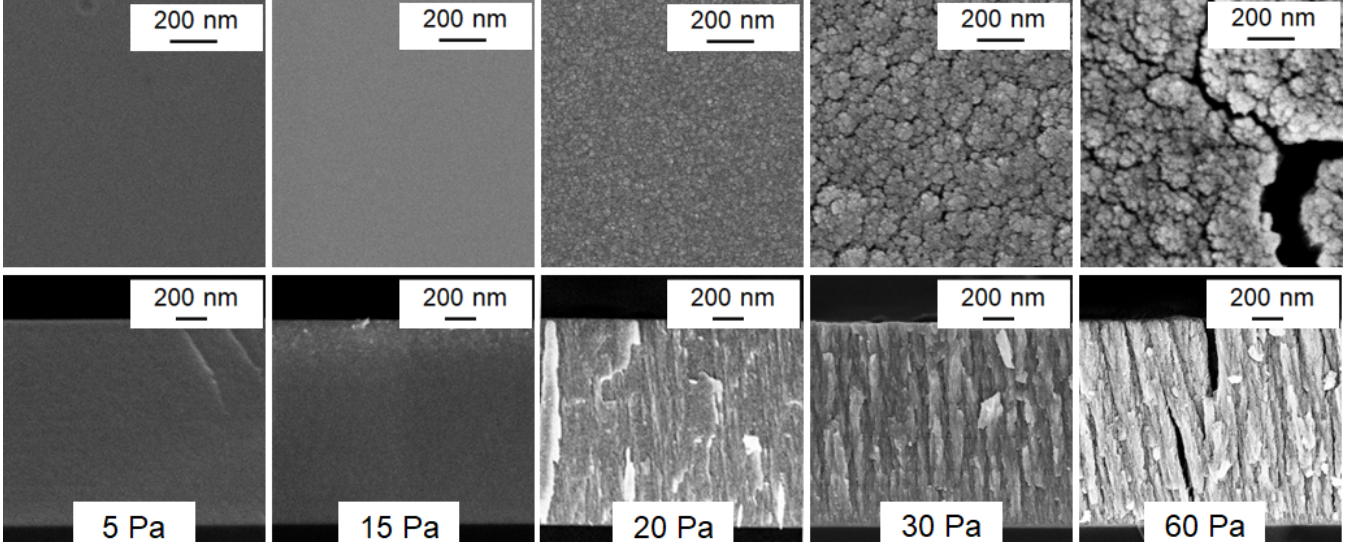


Figure 1: SEM top view and cross-section images of tungsten oxide coatings deposited by PLD at different O_2 background pressures.

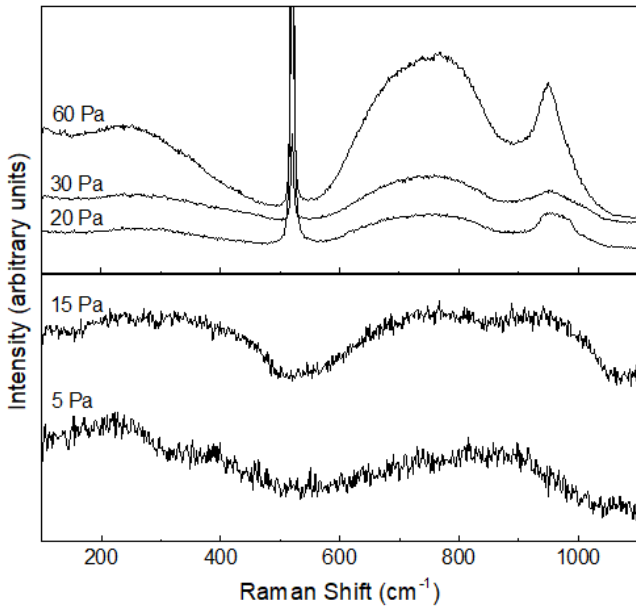


Figure 2: Raman spectra of tungsten oxide coatings deposited at different O_2 background pressures. The Si substrate peaks are at 521 cm^{-1} and at 960 cm^{-1} .

500 cm^{-1} , associated to the O-W-O bending modes, and a high frequency band in the range of $600 - 900\text{ cm}^{-1}$, attributed to the W-O stretching modes. This band-like spectrum underlines that all the as-deposited samples are amorphous [17, 18, 19, 26]. Despite this similar general aspect, some differences regarding band shapes and intensities can be seen in the spectra. Moreover, for deposition at pressure higher than 20 Pa the strong peak of silicon substrate at 521 cm^{-1} appears, revealing that such films are transparent oxide. On the contrary, for O_2 pressure below 20 Pa, the oxide formation regard only the sur-

face of the sample, while the rest of the films is metallic with no Raman signal and a strong laser absorption which does not reach the Si substrate. For this reason we call these tungsten-oxygen samples **a-W(O)**, to underline the amorphous metallic nature of the material, but with a significant oxygen content. Consistently, the transparent tungsten-oxide samples deposited at 20, 30 and 60 Pa are called **a-WO_{3-x}**, where $3 - x$ stands for possible stoichiometric defects. All the spectra present an additional contribution, a band at about 960 cm^{-1} , attributed in literature to the stretching mode of the W = O bonds at the surface of nanoclusters and void structures. It is thus related to material nanocrystallinity and porosity [17, 26]. This band is separated from the high frequency band only in the case of optically transparent films, but unfortunately it superimposes to the second order scattering of the Si substrate. Only at 60 Pa it evolves into a better defined peak, confirming the high degree of nanostructuration and the high surface-to-volume ratio of porous a-WO_{3-x} coatings.

The mass density (ρ) of the samples, estimated from the combination of weight measurements and SEM cross-section analysis, turns out to be strongly affected by the oxygen content. As it can be seen in figure 3, there is a strong linear dependence of ρ by the O/W ratio. In the case of a-W(O), ρ goes from 9.4 g cm^{-3} to 7 g cm^{-3} . For a-WO_{3-x}, instead, ρ is $\approx 5.6\text{ g cm}^{-3}$ at $O/W = 2.95$, 4.8 g cm^{-3} at $O/W = 3$ and 3.9 g cm^{-3} at $O/W = 3.1$. In these cases, the obtained values are below the bulk value of crystalline WO₃ (i.e. 7.1 g cm^{-3}) [27], remarking the higher porosity and amorphous structure that characterizes our samples. As a comparison, we reported in figure 3 the mass densities related to sputtered WO_x films that are commonly exploited for solar cells research and electrochromic devices [28]. As it can be seen, similar O/W ra-

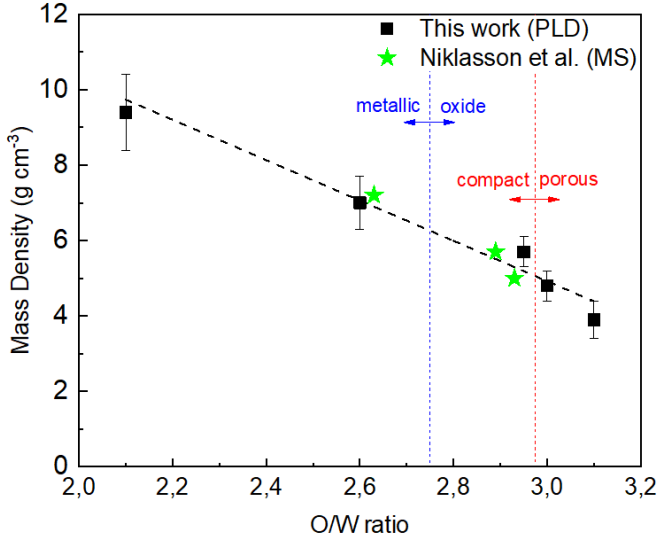


Figure 3: Measured mass density as function of the O/W ratio. Measured data are compared to literature values of WO_x films deposited by magnetro-sputtering [28]. The blue dotted-line separates metallic $a-W(O)$ samples from oxide $a-WO_{3-x}$ ones.

tios between sputtered and PLD films correspond to very similar mass densities. This is an important and somewhat surprising result since PLD and sputtering are characterized by very different ablated particles energy that, in turn, can deeply affect the structure of the film and its mass density. Since it is well known that ρ , disregarding the crystalline size, is the main parameter that affects the thermomechanical properties of a material, one could in principle expect very similar thermomechanical properties between PLD and sputtered films. This contributes to extend the results we obtain for PLD films to a more general family of tungsten-oxygen coatings. Moreover, it is evident that PLD, in turn, is able to strongly extend the range of possible O/W ratio.

3.2. Residual stresses and elastic moduli of as-deposited coatings

Residual stresses are evaluated by the substrate curvature method, by measuring the wafer curvature radius change at room temperature before and after the deposition of the film on the substrate. The obtained results are shown in figure 4. The values of σ_{res} are plotted versus the mass density ρ of the coatings. Two main regions can be observed, which are well separated by the change of film morphology: (i) compressive stresses in the case of compact samples, (ii) tensile stresses in the case of porous films. Moreover, inside the compressive region σ_{res} is affected by ρ , decreasing from -120 MPa in the case of metallic $a-W(O)$ to -50 MPa for $a-WO_{3-x}$, with ρ ranging from 9.4 to 5.6 $g\ cm^{-3}$. Accordingly, the tensile stresses magnitude decreases from ≈ 50 MPa to 20 MPa as ρ decreases from 4.8 to 3.9 $g\ cm^{-3}$.

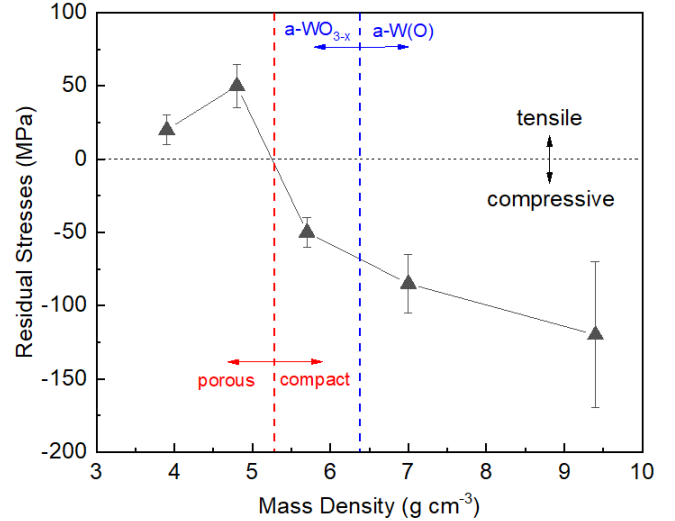


Figure 4: Measured residual stresses as function of mass density. The red line separates compact samples from porous ones, the blue one, instead, $a-W(O)$ from $a-WO_{3-x}$

The observed different nature of the residual stresses is directly associated to the PLD process and it can be described by considering general aspects regarding the growth of σ_{res} in PVD coatings. In general, the magnitude and the nature of σ_{res} is associated to various contributions, namely intrinsic stresses (σ_i) and thermal stresses (σ_{th}) that arise during deposition. In the particular case of PLD at room temperature intrinsic stresses prevail over the thermal counterpart. A detailed description of the nature of σ_i can be found elsewhere [29]. For the purpose of the present work, it is important to underline the fact that intrinsic stresses are determined by the sum of various contributions: (i) tensile stresses originating from the grain growth process (σ_{growth}), (ii) compressive stresses related to the adatoms diffusion to grain boundaries (σ_{diff}) and (iii) compressive stresses related to ion irradiation of the growing surface (σ_{ion}). Among them, σ_{ion} is commonly the dominant part when the energy of the ablated species is sufficiently high to promote knock-on displacements of surface adatoms (i.e. *atomic peening effect*). This leads to a consequent formation of defects and the growth of a compressive σ_i that can reach up to several GPa. In our case, the highest particles energy is found for compact high density coatings, which, consistently, are characterized by a compressive σ_{res} . When the energy decreases, σ_{ion} can be suppressed by the other contributions. In the case of porous films, the existing intercolumnar voids network in the structure due to pores presence can limit atoms mobility between columns. This inhibits grain boundaries motion, such that the tensile σ_{growth} prevails on the compressive σ_{diff} . This is again in accordance with our experimental evidence in the case of porous films, where σ_{res} is tensile.

This well distinct σ_{res} behavior can help in determining a

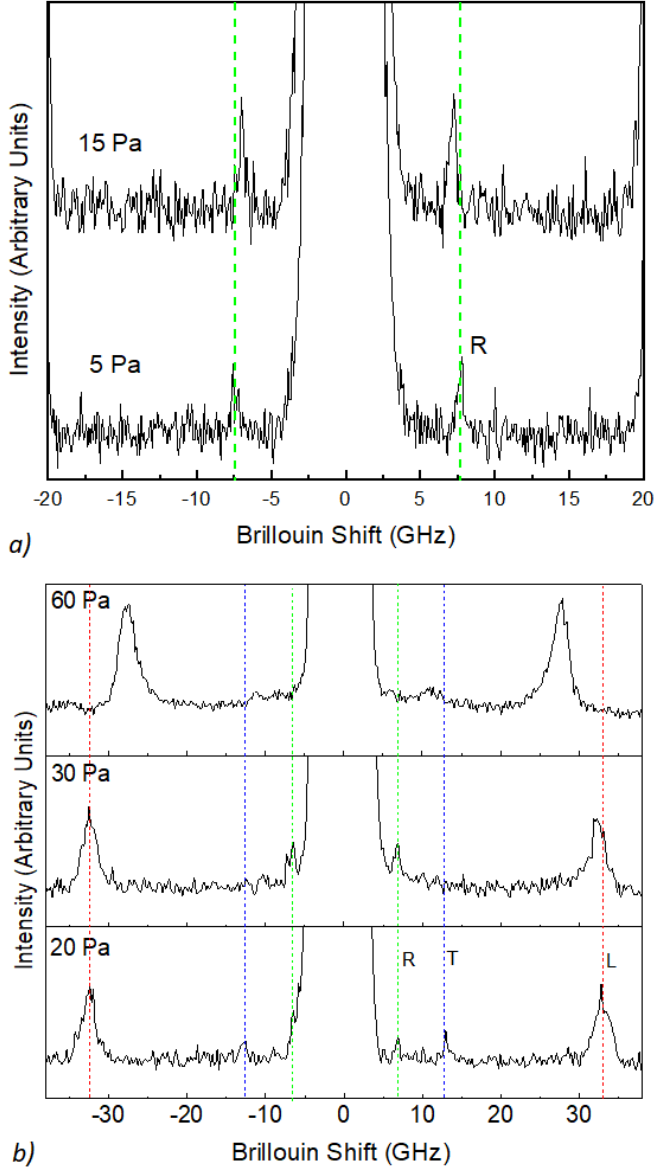


Figure 5: *a)* Brillouin spectra recorded for a -W(O) coatings at an angle of incidence $\theta = 60^\circ$. *b)* Brillouin spectra recorded for a -WO_{3-x} coatings at an angle of incidence $\theta = 60^\circ$. R = Rayleigh mode, T transverse bulk mode, L = longitudinal bulk mode.

”safety” region for the choice of the films for various applications. Indeed, a compressive residual stress is known to be beneficial for the mechanical behavior of the coatings, for example by increasing the cracks, wear and corrosion resistance, which are fundamental requirements for applications where high temperatures or external loads are applied. Tensile stresses, on the contrary, are generally undesirable as they decrease fatigue strength and life, increase crack propagation and lower resistance to environmentally assisted cracking. The higher cracking probability of tensile coatings is well highlighted by SEM images in figure 1, where a high density of through-thickness cracks is found

at 60 Pa.

The elastic moduli of the coatings are then determined by Brillouin spectroscopy. As discussed in section 2.3, the moduli are derived under the isotropic homogeneous condition. This condition is well satisfied for compact amorphous coatings. However, tree-like nanostructure in porous samples can induce a substantial anisotropy to the mechanical properties of the films, such as the in-plane properties can differ from the out-of-plane ones. We have already considered possible anisotropy effects on the elastic moduli of nanostructured tungsten films measured by Brillouin spectroscopy in our past work [20]. The elastic moduli reported here for porous samples, computed under the isotropic condition, can be seen as lower bounds for the real anisotropic moduli, these moduli being the ones of an equivalent homogeneous material which has the same in-plane and out-of-plane properties.

Brillouin spectra recorded for a -W(O) and a -WO_{3-x} samples are shown in figure 5a and 5b respectively. All the spectra are recorded at a laser angle of incidence $\theta = 60^\circ$. As it can be seen, in the case of metallic a -W(O) coatings, only a low frequency mode can be detected. This mode is associated to the surface Rayleigh wave (R) of the film. In the case of optically transparent WO_{3-x}, instead, in addition to the low frequency R mode, two additional peaks become clearly visible: the mid frequency transverse bulk acoustic wave (T) and the high frequency longitudinal bulk acoustic wave (L). As it can be seen, while the spectra obtained at 20 and 30 Pa are quite similar, at 60 Pa an evident shift of the modes towards lower frequencies is detected. The position of these peaks in the spectrum depends on different factors, such as the elastic properties, mass density and the refractive index. As already mentioned in section 2.2, the observed peaks shift can be thus attributed to a variation of all these properties. In addition, at 60 Pa the R mode disappears. This is due to the really open porous morphology, that does not support surface waves propagation.

In the specific case of a -W(O) coatings, the thickness of the sample (i.e. $\approx 3 \mu\text{m}$) is such that the coatings behave like a semi-infinite medium, the displacement field associated to SAWs being completely confined within the films (i.e. no energy radiated into the substrate). This has two main consequences. On one hand, the SAWs are not dispersive (i.e. the frequency of the modes does not depend on k), such that, in principle, the information from only one measurement at one incidence angle θ could be sufficient. On the other hand, this limits the number of possible detectable SAWs. For a -W(O) films, only the elastic information carried by the R wave can be exploited, following the procedure described in section 2.2, thus limiting the accuracy in the estimation of the elastic moduli. In the case of a -WO_{3-x} films, instead, the elastic moduli can be derived directly from the bulk peaks positions through equations 1, 2 and 3. In order to do that, the refractive index of the films must be known. In this case, the simultaneous presence of the R and T waves, observed

O ₂ Pressure (Pa)	O/W	ρ (g cm ⁻³)	thickness (μ m)	n (532 nm)	σ_{res} (MPa)	Elastic modulus (GPa)
5	2.1	9.4	3.1 \pm 0.32	-	- 120 \pm 50	125 \pm 20
15	2.6	7	3.1 \pm 0.35	-	- 85 \pm 25	74 \pm 10
20	2.95	5.7	3.3 \pm 0.4	1.88 \pm 0.1	- 50 \pm 5	72 \pm 8
30	\approx 3	4.8	3.3 \pm 0.4	1.68 \pm 0.08	50 \pm 7	68 \pm 5
60	3.1	3.9	3.2 \pm 0.35	1.49 \pm 0.1	20 \pm 5	43 \pm 8

Table 1: O/W stoichiometric ratio, mass density, thickness, refractive index (at 532 nm), residual stress (σ_{res}) and elastic modulus (E) of the coatings.

at 20 Pa and 30 Pa, is exploited to derive a consistent estimation of n . Due to its predominantly shear nature, the Rayleigh velocity (v_R) can be approximated in terms of v_T as $v_R \approx f(\nu)v_T$ [30], where $f(\nu) = \frac{0.862+1.14\nu}{1+\nu}$, ν being the Poisson's ratio of the film. v_R can be easily extracted from the frequency shift observed in the spectrum, and without needing the value of n as [24]:

$$v_R = \frac{\Delta\omega_R\lambda_0}{4\pi\sin\theta} \quad (6)$$

In the case of W based materials, the Poisson's ratio has been found in the range between 0.28 and 0.45 [20]. Considering $f(\nu) = 0.933 \pm 0.015$, $v_T \approx 0.933v_R$ introduces only a 1.6% error in the approximation of n . For this reason, we compute v_R from the R peak position in the spectrum (see fig. 5b), and then we substitute it in equation 3 to extract an estimation of n . This procedure is done for the samples deposited at 20 and 30 Pa, where the R and T modes are simultaneously present. At 60 Pa, the R mode is not present. Since it is reasonable to consider that the polarizability of a-WO_{3-x} does not change between 20 Pa and 60Pa (e.g. no effects related to crystallization), n can be consistently estimated by means of the well known Lorenz-Lorentz correlation [31]:

$$\rho_{60} = \rho_{20} \frac{n_{20}^2 - 1}{n_{60}^2 - 1} \frac{n_{60}^2 + 1}{n_{20}^2 + 1} \quad (7)$$

where ρ_{20} and ρ_{60} are the mass densities of the amorphous coatings at 20 and 60 Pa respectively, while n_{20} and n_{60} the corresponding refractive indexes. The obtained values of n at 532 nm are summarized in table 1. For example, in the case of compact a-WO_{3-x} we obtain a refractive index of ≈ 1.88 which is in good agreement with the ones reported in literature for compact amorphous WO₃ films (i.e. ≈ 1.9) [27, 32].

From the estimation of n at 532 nm, C_{11} , C_{44} and all the elastic moduli are finally obtained. Figure 6 summarizes the values of the elastic Young modulus (E), the shear modulus (G) and the shear to bulk modulus ratio (G/K), which, in particular, can be seen as an index of local ductility of the material [20]. In figure 6a the moduli are plotted as function of ρ , while in figure 6b versus the O/W ratio. As it can be seen, a strong dependence of the mod-

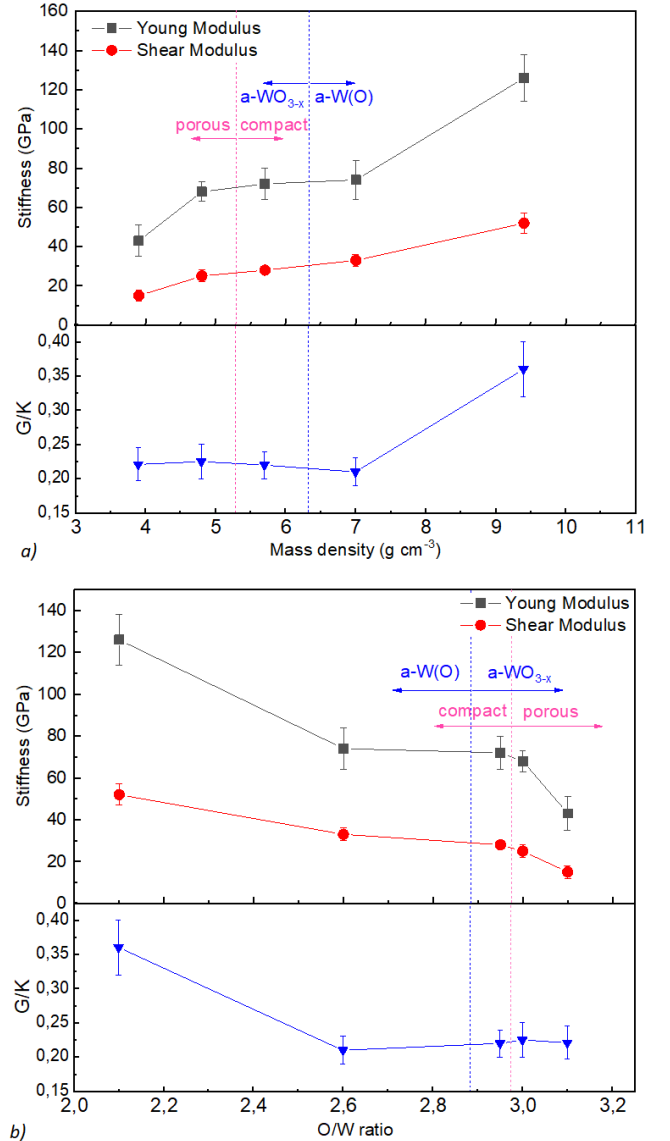


Figure 6: Elastic moduli the coatings. a) Young Modulus E , shear modulus G and G/K ratio as function of film mass density. b) the same properties as function of the stoichiometric ratio.

uli by ρ and the O/W ratio is found: as ρ decreases and O/W increases the stiffness drastically decreases. Metal-

lic a-W(O) coatings are characterized by a higher stiffness with respect to the oxide counterpart. In the metallic region E goes from ≈ 125 GPa to ≈ 74 GPa, coherently G drops from 52 GPa to 33 GPa. G/K , instead, goes from ≈ 0.36 to ≈ 0.21 . This is a non-obvious trend, since from SEM and Raman analysis there is not an appreciable difference between these samples. At $\rho = 7 \text{ g cm}^{-3}$, which corresponds to $O/W = 2.6$, a plateau of the moduli is reached: the material changes its chemical configuration, by forming tungsten-oxide, but the properties are not affected even if ρ decreases between the samples. In particular, E remains between 68 and 72 GPa, G between 25 and 28 GPa and $G/K \approx 0.21$. We can thus speculate that there is a consistent interplay between the variation of the chemical surround, attributed to the different W - O bond strength which characterizes tungsten oxide, and the decrease of mass density that confers the same stiffness to very different materials. Finally, when evident intercolumnar pores appear a further little decrease is found for E and G at 60 Pa (i.e. $E = 43$ GPa, $G = 16$ GPa), such that the mass density is the main parameter in determining the elastic moduli.

The stiffness observed for metallic a-W(O) films is lower than the one proper of metallic amorphous-like W (i.e. $E = 150$ GPa, $G = 50$ GPa [20]), as it is the one of a-WO_{3-x} in comparison with cubic WO₃ (i.e. $E = 258$ GPa, $G = 100$ GPa, $G/K = 0.48$ [33]). In the former case, the observed softening is related to the increase of the retained oxygen ratio, that goes from 0.4 for metallic amorphous-like tungsten [20] to 2.6 for a-W(O), and to a corresponding decrease of film density. In the latter case, instead, it can be attributed to the specific amorphous structure of the film. As a result of the loss of the long range order proper of crystalline materials, the interatomic potential in the case of amorphous materials can be lowered. This, in turn, can be associated to a higher mean interatomic distance, which means a lower mean interatomic binding energy, so lower elastic moduli [34]. However, this can confer the material some peculiar properties. For example, the drop observed for G/K is related to an increase of local ductility, so to a higher ability of the material to locally allocate shear flow. In these terms, a-WO_{3-x} films can be macroscopically brittle but microscopically capable of sustaining shear flow [35].

These results can be compared to the few ones reported in literature for PVD WO₃ coatings [14, 15, 36]. *Parreira et al.* [15] found a Young modulus of amorphous WO₃ films of ≈ 100 GPa, which is slightly higher than our values. For lower oxygen contents (i.e. O/W below 3) the discrepancy is evidently less pronounced: they found E varying between 170 and 100 GPa for O/W ratios between 2 and 2.6, which corresponds to the E values we measured for a-W(O) coatings of 125 GPa and 74 GPa. *Polcar et al.* [36] and *Carrejo et al.* [14], instead, report higher Young modulus (i.e. between 110 and 164 GPa) for compact amorphous WO₃ coatings. Nevertheless, the correlation between all these results is difficult since there

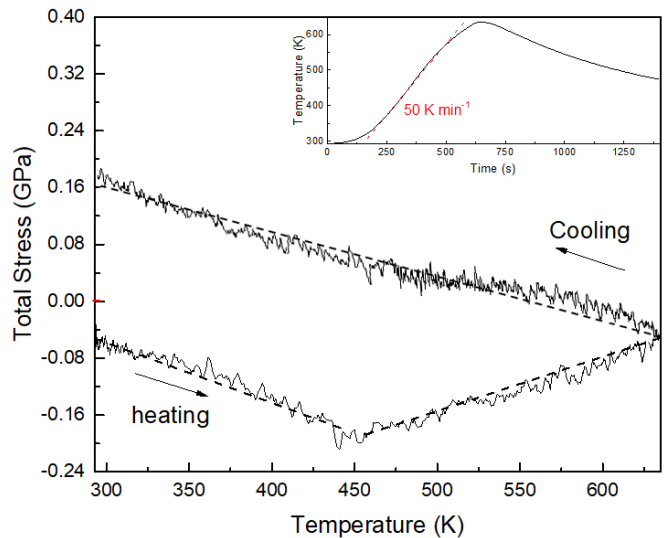


Figure 7: Film stress evolution during annealing evaluated by the SC method. The black dotted line represents a linear fit of the mean value of the stress.

is no information about the material mass density, that, as already mentioned, severely affects the elastic properties of the material. However, the authors show an evident softening of the coatings with O₂ enrichment in the deposition atmosphere, which is in agreement with our results. The previous mechanical characterization highlighted that compact a-WO_{3-x} films (deposited at 20 Pa of O) are characterized by interesting mechanical properties, such as compressive residual stresses and high local ductility, which can be fruitful for a wide range of applications. For this reason, they are chosen as the reference samples for successive characterizations. We thus characterize the CTE of as-deposited a-WO_{3-x} films and the evolution of σ_f during thermal treatments, as well as we investigate the influence of different annealing temperatures on the morphology, the structure and on the elastic moduli.

3.3. Coefficient of thermal expansion and stress evolution of a-WO_{3-x} coatings

The CTE of a-WO_{3-x} films is determined following the procedure described in section 2.3. This requires the monitoring of the film-substrate curvature radius during temperature ramps. The standard thermal treatment adopted to this purpose is shown in the inset of figure 7. Here, the total film stress σ_f is monitored during heating and cooling. The linear fit of the mean value of the stress (i.e. the dotted line) during the first heating steps is then exploited to derive the CTE of the film. Considering equation 5, the slope of the dotted line is equal to $\frac{d\sigma_f}{dT} = \frac{E}{1-\nu}(CTE_f - CTE_{Si})$. In this way, we obtain a mean CTE of $8.6 \cdot 10^{-6} \text{ K}^{-1}$ between 273 - 450 K. Very few information about the CTE of tungsten-oxide is available in literature, but it is known that tungsten-oxide materials can have very different thermal expansion

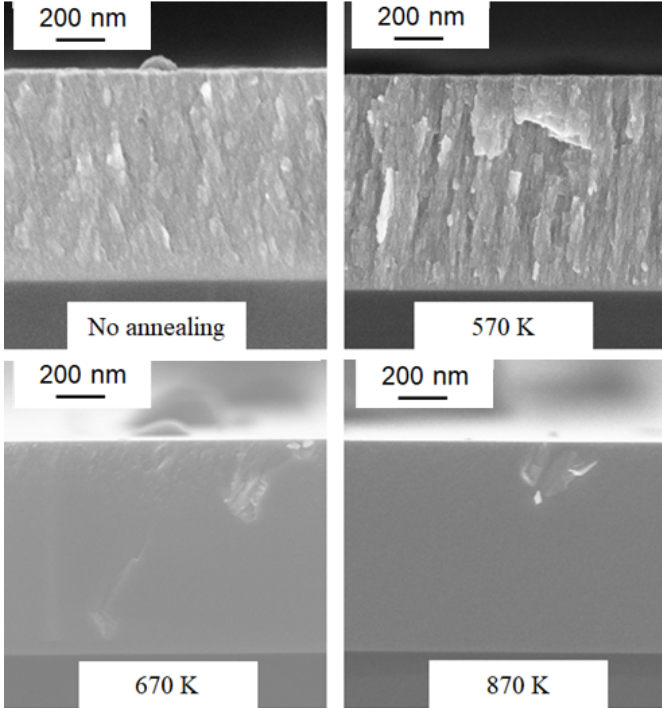


Figure 8: SEM images of annealed $a\text{-WO}_{3-x}$ samples for 1 hour in vacuum at different temperatures.

coefficients, that are strongly correlated with the specific stoichiometry and can even be negative at high temperatures. For example, the CTE at room temperature can vary from $1.3 \cdot 10^{-6} \text{ K}^{-1}$ in the case of $\text{W}_{18}\text{O}_{49}$ to $3.3 \cdot 10^{-6} \text{ K}^{-1}$ for WO_2 and between 8 and $15 \cdot 10^{-6} \text{ K}^{-1}$ for WO_3 [37, 38, 39]. Our computed value is higher than the one of the Si substrate (i.e. $2.6 \cdot 10^{-6} \text{ K}^{-1}$), which explains the negative slope of the linear fit, and it is in agreement with the range of values reported in literature. Differences between literature values and our result can be attributed to a different structure of the material (e.g. crystalline vs amorphous) and possible stoichiometric defects.

As it can be seen in figure 7 a compressive residual stress is initially developed during the heating cycle for temperatures up to 450 K. The stress magnitude increases, as expected, linearly with heating temperature up to 450 K. However, after 450 K, which corresponds to a stress of $\approx -180 \text{ MPa}$, the total stress begins to reverse its sign becoming more tensile. This is a strong evidence of the beginning of some structural evolution. The tensile nature of the developed stress can be associated to the observed volume shrinkage which, in turn, relates to the beginning of diffusion and grain growth processes [29]. These processes continue until the maximum temperature is reached. Upon cooling, instead, the tensile stress associated to the coefficient of thermal expansion mismatch between the film and the substrate increases linearly with decreasing temperature. The linear trend upon cooling shows almost the same slope of the heating cycle. This slope, as already

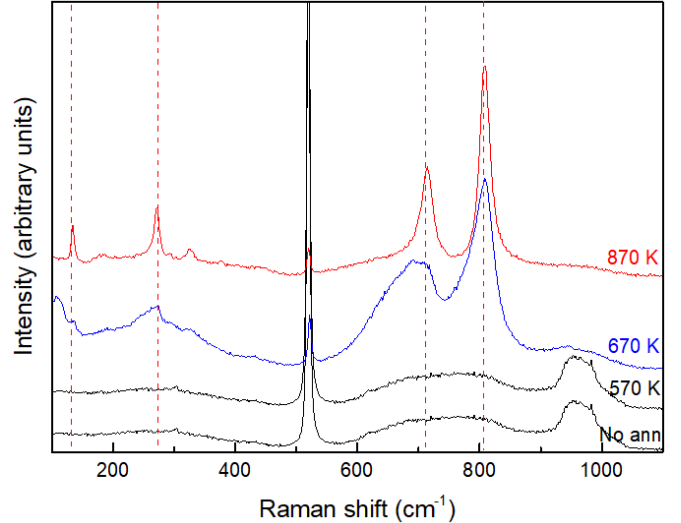


Figure 9: Raman spectra of annealed $a\text{-WO}_{3-x}$ samples. The red dotted lines correspond to the principal peaks proper of γ monoclinic WO_3 . Si substrate peaks are present at 521 cm^{-1} and at 960 cm^{-1} .

mentioned, is related to the CTE and the elastic modulus of the coating. For this reason, we can assume that no irreversible changes of these macroscopic properties have been induced by the fast thermal treatment, the kinetic of structural evolution being probably slower than the total annealing time. What changes is the value of σ_f . After the thermal cycle, the film is found in a tensile state of stress. This underlines that σ_{res} relaxation has occurred, inducing local structure reorganization associated to defects diffusion at relatively low temperatures.

3.4. Thermal annealing of $a\text{-WO}_{3-x}$ coatings

Temperature induced effects on $a\text{-WO}_{3-x}$ films is investigated by vacuum annealing treatments performed between 570 K and 870 K. SEM cross section images of annealed $a\text{-WO}_{3-x}$ coatings are shown in figure 8. Up to 570 K no substantial morphological changes are visible. Starting from 670 K, instead, SEM analysis clearly show a morphology modification. The compact nanostructured morphology of as-deposited $a\text{-WO}_{3-x}$ evolves into a featureless, more compact one. This can be related to the annealing driven structural reorganization process, which, in turn, suggests that around 670 K crystallization occurs. SEM cross section images also show a decrease by about 20% of film thickness starting from 670 K. The thickness, indeed, goes from $3.3 \mu\text{m}$ to $\approx 2.7 \mu$ at 670 K. This, in turn, is associated with an increase of film mass density, that goes from the as-deposited value of 5.7 g cm^{-3} to $\approx 7 \text{ g cm}^{-3}$ above 670 K.

Raman spectroscopy is exploited to better highlight the observed crystallization process. The obtained spectra are shown in figure 9. Up to 570 K, no remarkable differences of the spectrum with respect to the as-deposited case

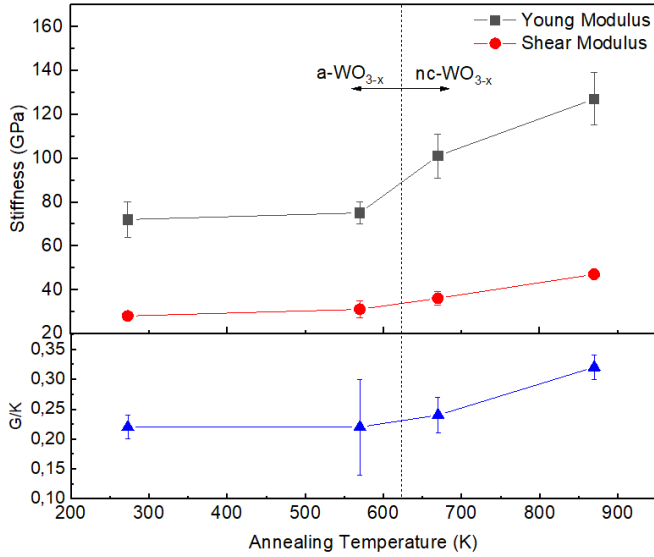


Figure 10: Elastic moduli of annealed $a\text{-WO}_{3-x}$ films.

can be detected. This is in agreement with SEM analysis, which does not report a strong variation of the film structure and morphology. At 670 K, instead, several new peaks become visible. These peaks grow in correspondence of 133 cm^{-1} , 273 cm^{-1} , 715 cm^{-1} and 805 cm^{-1} , which correspond to the principal peaks of the crystalline γ monoclinic phase of WO_3 [40]. The observed peaks width, in particular the width of the peak at 715 cm^{-1} , suggests that, at this temperature, it is still present a consistent amount of amorphous structure such that the crystallization process is not completed. This agrees with the fact that at 870 K definitely sharper peaks are found. Moreover, the positions of these peaks are slightly shifted with respect to the ones of $\gamma\text{-WO}_3$. This can be attributed to different factors, such as internal stresses developed during annealing or stoichiometry defects. For the former case, as highlighted by stress evolution measurements of figure 7, the growth of a new crystalline phase in an amorphous matrix can lead to the development of a high internal state of stress associated to atoms diffusion, grains coalescence and growth. For the latter, EDXS analysis performed on annealed samples confirm a slight reduction of the O/W ratio for $a\text{-WO}_{3-x}$ from ≈ 2.95 down to 2.88. This could suggest that a small part of the total amount of O_2 is only trapped in the as deposited film and can desorb at relevant temperatures.

The observed crystallization affects the mechanical properties of the films, which are assessed by Brillouin analysis following the same procedure adopted for $a\text{-WO}_{3-x}$ samples described in the previous section. The obtained elastic moduli are summarized in figure 10. As expected, if annealing is performed at 570 K only a slight increase of material stiffness is observed. At 670 K, instead, when crystallization begins, $E = 101\text{ GPa}$, $G = 36\text{ GPa}$ and $G/K = 0.24$, with a consequent increase by about 36% of E with respect to the as-deposited condition. These

properties can be the result, in agreement with what we found in [20], of the properties of an amorphous matrix in which nanocrystals are embedded. Finally, when the γ monoclinic WO_3 phase is better defined at 870 K, a further increase of the moduli is detected (i.e. $E = 127\text{ GPa}$, $G = 50\text{ GPa}$ and $G/K = 0.38$). These results are in accordance with what we observed in figure 7 concerning the total stress evolution. We determined the relaxation temperature T_R to be at 450 K, and we found that even if we rapidly heat the sample at temperatures $T > T_R$ no changes of the macroscopic properties are observed. This agrees with the slight stiffening observed at 570 K. Coherently, only 1 hour annealing treatments at 670 K can alter significantly the nanostructure and the properties of the material. The corresponding stiffening process is, in turn, attributed to different competitive processes, such as structural relaxation, free volume annihilation and short-range ordering (i.e. nano-crystals formation), which can increase the interatomic potential and consequently the elastic moduli of the material [41].

4. Conclusions

In this work, we investigated the thermomechanical properties of different systems of amorphous tungsten-oxygen and tungsten-oxide coatings. The samples were deposited by PLD, which allowed us to finely tailor the morphology, the structure and the composition of the films in order to have a broad family of samples. In this way, we could derive the relationship between these properties and the thermomechanical ones, which is not easily measurable and can be fruitful for many applications of this kind of coating materials where the films are required to operate at high temperatures or external loads (e.g. thermophotovoltaic, solar cells, electronics).

In particular, the mechanical properties of the as-deposited films, (i.e. the elastic moduli and the residual stress) resulted to be simultaneously influenced by the morphology and the O/W ratio: as the films become less dense and rich of oxygen, the stiffness and residual stresses linearly decrease. However, for ρ between $4.8 - 7\text{ g cm}^{-3}$ and O/W ratio between 2.6 and 3 the stiffness remains constant, probably due to an interplay between a variation of bonds strength related to the oxide formation and the loss of mass density. Among tungsten-oxide coatings, compact $a\text{-WO}_{3-x}$ films showed the most promising as deposited mechanical properties, with a moderate stiffness, compressive residual stresses and a relatively high ability to locally allocate shear flow, which can be desired for their applications under external thermal or mechanical loads. The quite high CTE and a quite low relaxation temperature must be considered for their use in high temperature applications. Crystallization into the monoclinic $\gamma\text{-WO}_3$ phase starts at 670 K, with a consequent strong crystallization induced stiffening and a decrease of local ductility. The lower observed relaxation temperature (i.e. 450

K) suggests that possible structural relaxation and diffusion processes already begin at temperatures well below the determined annealing temperature, without affecting the overall properties of the material. Since the knowledge of annealing kinetics can be crucial to determine the evolution of films properties under high temperatures, this type of analysis will require further investigation.

Acknowledgments

This work has been carried out within the framework of the MISE-ENEA ‘*Accordo di Programma*’ (AdP), PAR2015 and PAR2016. The views and opinions expressed herein do not necessarily reflect those of the European Commission. The research leading to these results has also received funding from the European Research Council Consolidator Grant ENSURE (ERC-2014-CoG No. 647554).

References

- [1] H. Zheng, J. Z. Ou, M. S. Strano, R. B. Kaner, A. Mitchell and K. Kalantar-zadeh, Nanostructured Tungsten Oxide - Properties, Synthesis, and Applications, *Adv. Funct. Mater.* 2011, 21, 2175-2196.
- [2] S. Wang, W. Fan, Z. Liu, A. Yu and X. Jiang, Advances on tungsten oxide based photochromic materials: strategies to improve their photochromic properties, *J. Mater. Chem. C*, 2018, 6, 191.
- [3] C. G. Granqvist, Transparent conductive electrodes for electrochromic devices: A review, *Appl. Phys. A*, 1993, 57:19.
- [4] O.R. Nunez, A.J. Moreno Tarango, N.R. Murphy, L.C. Phinney, K. Hossain, C.V. Ramana, Physical characterization of sputter-deposited amorphous tungsten oxynitride thin films, *Thin Solid Films* 596 (2015) 160-166.
- [5] B. Abdel Samad, P.V. Ashrit, Optimization of mixed conductivity through nanostructure control in WO₃ thin films, *Thin Solid Films* 636 (2017) 717-722.
- [6] A. Karuppasamy, A. Subrahmanyam, Studies on electrochromic smart windows based on titanium doped WO₃ thin films, *Thin Solid Films* 516 (2007) 175-178.
- [7] W. Li, P. Da, Y. Zhang, Y. Wang, X. Lin, X. Gong, G. Zheng, WO₃ nanoflakes for enhanced photoelectrochemical conversion, *ACS Nano* 8 (2014) 11770-11777.
- [8] S. Shin, H. Soo Han, J. S. Kim, I. J. Park, M. H. Lee, K. S. Hong and I. S. Cho, A tree-like nanoporous WO₃ photoanode with enhanced charge transport efficiency for photoelectrochemical water oxidation, *J. Mater. Chem. A* 3 (2015) 12920.
- [9] S. K. Deb, Opportunities and challenges in science and technology of WO₃ for electrochromic and related applications, *Sol. Energ. Mat. Sol.* 2008, 92, 245.
- [10] T. Kikuchi, J. Kawashima, S. Natsui, R. O. Suzuki, Fabrication of porous tungsten oxide via anodizing in an ammonium nitrate/ethylene glycol/water mixture for visible light-driven photocatalyst, *Appl. Surf. Sci.* 422 (2017) 130-137.
- [11] D. Dellasega, S. M. Pietralunga, A. Pezzoli, V. Russo, L. Nasi, et al., Tungsten oxide nanowires grown on amorphous-like tungsten films, *Nanotechnology* 26 (2015) 365601.
- [12] R. Seelaboyina, Tungsten oxide nanowire synthesis from amorphous-like tungsten films, *Nanotechnology* 27 (2016) 112502.
- [13] Dip. K.Nandi, Shaibal K.Sarkar, Atomic Layer Deposition of Tungsten Oxide for Solar Cell Application, *Energy Procedia* 54, 782-788 (2014).
- [14] J. L. Enriquez-Carrejo, M. A. Ramos, J. Mireles-Jr-Garcia, A. Hurtado-Macias, Nano-mechanical and structural study of WO₃ thin films, *Thin Solid Films* 606 (2016) 148-154.
- [15] N.M.G. Parreira, N.J.M. Carvalho and A. Cavaleiro, Synthesis, structural and mechanical characterization of sputtered tungsten oxide coatings, *Thin Solid Films* 510 (2006) 191-196.
- [16] M. M. Hasan, A. S. M. A. Haseeb and H. H. Masjuki, Structural and mechanical properties of nanostructured tungsten oxide thin films, *Surface Engineering* 28:10 (2012) 778-785.
- [17] A. Pezzoli, D. Dellasega, V. Russo, A. Gallo, P.A. Zeijlmans van Emmichoven, M. Passoni, Thermal annealing and exposure to divertor-like deuterium plasma of tailored tungsten oxide coatings, *J. Nucl. Mater.* 463 (2015) 1041-1044.
- [18] A. Baserga, V. Russo, F. Di Fonzo, A. Bailini, D. Cattaneo, C.S. Casari, A. Li Bassi, C.E. Bottani, Nanostructured tungsten oxide with controlled properties: Synthesis and Raman characterization, *Thin Solid Films* 515 (2007) 6465-6469.
- [19] A. Bailini, F. Di Fonzo, M. Fusi, C.S. Casari, A. Li Bassi, V. Russo, A. Baserga, C.E. Bottani, Pulsed laser deposition of tungsten and tungsten oxide thin films with tailored structure at the nano- and mesoscale, *Applied Surface Science* 253 (2007) 8130-8135.
- [20] E. Besozzi, D. Dellasega, A. Pezzoli, C. Conti, M. Passoni, M.G. Beghi, Amorphous, ultra-nano- and nano-crystalline tungsten-based coatings grown by Pulsed Laser Deposition: mechanical characterization by Surface Brillouin Spectroscopy, *Materials and Design* 106 (2016) 14-21.
- [21] D. Dellasega, V. Russo, A. Pezzoli, C. Conti, N. Lecis, E. Besozzi, M. Beghi, C.E. Bottani, M. Passoni, Boron films produced by high energy Pulsed Laser Deposition, *Materials and Design* 134 (2017) 35-43.
- [22] E. Besozzi, D. Dellasega, A. Pezzoli, A. Mantegazza, M. Passoni, M.G. Beghi, Coefficient of thermal expansion of nanostructured tungsten based coatings assessed by substrate curvature method, *Materials and Design* 137 (2018) 192-203.
- [23] F.G. Ferre, E. Bertarelli, A. Chiodoni, D. Carnelli, D. Gastaldi, P. Vena, M.G. Beghi, F. Di Fonzo, The mechanical properties of a nanocrystalline Al₂O₃/a-Al₂O₃ composite coating measured by nanoindentation and Brillouin spectroscopy, *Acta Mater.* 61 (2013) 2662-2670.
- [24] T. Kundu, Mechanics of elastic waves and ultrasonic nondestructive evaluation, in *Ultrasonic Nondestructive Evaluation*, edited by T. Kundu, CRC Press, Boca Raton, FL, (2004), chapter 10.
- [25] G. Stoney, The tension of metallic films deposited by electrolysis, *Proc. R. Soc. Lond. Ser. A Contain. Pap. Math. Phys. Character*, 82 (553) pp. 172-175 (1909).
- [26] F. Di Fonzo et al., Synthesis and characterization of tungsten and tungsten oxide nanostructured films, *Catalysis Today* 116(1):69 - 73, 2006.
- [27] K. von Rottkay, M. Rubin, S.-J. Wen, Optical indices of electrochromic tungsten oxide, *Thin Solid Films* 306 (1997)10-16.
- [28] G. A. Niklasson and C. G. Granqvist, Electrochromics for smart windows: thin films of tungsten oxide and nickel oxide, and devices based on these, *J. Mater. Chem.* 17 (2007) 127-156.
- [29] R. Daniel, K.J. Martinschitz, J. Keckes, C. Mitterer, The origin of stresses in magnetron-sputtered thin films with zone T structures, *Acta Materialia* 58 (2010) 2621-2633.
- [30] L. B. Freund *Dynamic Fracture Mechanics*, Cambridge University Press. p. 83. ISBN 978-0521629225 (1998).
- [31] E. Washizu, A. Yamamoto, Y. Abe, M. Kawamura, K. Sasaki, *Solid State Ionics* 165 (2003) 175.
- [32] X. Sun, Z. Liu, H. Cao, Effects of film density on electrochromic tungsten oxide thin films deposited by reactive dc-pulsed magnetron sputtering, *Journal of Alloys and Compounds* 504S (2010) S418-S421.
- [33] Liu X, Fan H-Q, Electronic structure, elasticity, Debye temperature and anisotropy of cubic WO₃ from first-principles calculation. *R. Soc. open sci.* 5, (2018) 171921.
- [34] L. Liang, M. Li, F. Qin and Y. Wei, Temperature effect on elastic modulus of thin films and nanocrystals, *Philosophical*

- Magazine 9, 8, (2013) 574 - 583.
- [35] C.A. Schuh, T.C. Hufnagel, U. Ramamurty, Mechanical behavior of amorphous alloys, *Acta Mater.* 55 (2007) 4067-4109.
 - [36] T. Polcar, N.M.G. Parreira, A. Cavaleiro, Tungsten oxide with different oxygen contents: Sliding properties, *Vacuum* 81 (2007) 1426-1429.
 - [37] Weast RC. *CRC Handbook of Chemistry and Physics*. Boca Raton: CRC Press; 1988.
 - [38] T. Tokunaga, T. Kawamoto, K. Tanaka, N. Nakamura, Y. Hayashi, K. Sasaki, K. Kuroda and T. Yamamoto, Growth and structure analysis of tungsten oxide nanorods using environmental TEM, *Nanoscale Res Lett.* 7(1), 85 (2012).
 - [39] T. Takamori, Thermal Expansion Characteristics of Polycrystalline Tungsten Oxides, *Journal of the American Ceramic Society*, 47(10), 534-535 (1964).
 - [40] S. Hayashi et al., Phase Transitions in Gas-Evaporated WO_3 Microcrystals: A Raman Study, *J. Phys. Soc. Jpn.* 61, 916 (1992).
 - [41] G. Ouyang, X. L. Li, X. Tan and G. W. Yang, Size-induced strain and stiffness of nanocrystals, *Appl. Phys. Lett.* 89, 031904 (2006).